

## *Ab initio* molecular dynamics simulations of low-energy recoil events in ThO<sub>2</sub>, CeO<sub>2</sub>, and ZrO<sub>2</sub>

H. Y. Xiao,<sup>1</sup> Y. Zhang,<sup>1,2</sup> and W. J. Weber<sup>1,2</sup><sup>1</sup>*Department of Materials Science and Engineering, University of Tennessee, Knoxville, Tennessee 37996, USA*<sup>2</sup>*Materials Science and Technology Division, Oak Ridge National Laboratory, Oak Ridge, Tennessee 37831, USA*

(Received 17 March 2012; revised manuscript received 28 June 2012; published 13 August 2012)

*Ab initio* molecular dynamics simulations of low-energy recoil events in ThO<sub>2</sub>, CeO<sub>2</sub>, and ZrO<sub>2</sub> have been carried out to determine the threshold displacement energies, resulting defect configurations, dynamics of defect generation, and role of charge transfer during the process. The results reveal that, in most cases, these fluorite structure oxides exhibit a similar response to low-energy recoils. A variety of different defect configurations are created, consisting mainly of vacancies and interstitials. Charge transfer occurs during the dynamic displacement process. Local charge redistribution leads to cation and O vacancies being negatively and positively charged, respectively. Likewise, due to charge redistribution, the cation and O interstitials are less positively and negatively charged, respectively, than the ions on lattice sites in perfect MO<sub>2</sub>.

DOI: [10.1103/PhysRevB.86.054109](https://doi.org/10.1103/PhysRevB.86.054109)

PACS number(s): 61.72.Cc

### I. INTRODUCTION

Cubic urania (UO<sub>2</sub>), thoria (ThO<sub>2</sub>), ceria (CeO<sub>2</sub>), and zirconia (ZrO<sub>2</sub>) not only share the same fluorite structure in which the cations are lying in an fcc sublattice while the anions are in a cubic sublattice, but also exhibit similar thermophysical properties. These oxides are generally known to be highly radiation resistant and, therefore, are materials of great interest for nuclear applications: UO<sub>2</sub> is the primary nuclear fuel in most nuclear power plants;<sup>1</sup> ThO<sub>2</sub> has demonstrated potential for a proliferation-resistant nuclear fuel cycle;<sup>2</sup> CeO<sub>2</sub> is often used as a nonradioactive surrogate for UO<sub>2</sub> and PuO<sub>2</sub>;<sup>3–6</sup> and ZrO<sub>2</sub> has been proposed as an inert matrix for transmutation of actinides in advanced fuel cycles.<sup>7,8</sup> Consequently, numerous experimental studies have been carried out on these oxides in order to investigate their behavior under irradiation.<sup>9–13</sup>

Self-radiation from  $\alpha$  decay and fission as well as irradiation with neutrons, ions, and electrons, result in the production of defects from energy transfer through scattering collisions with atoms in the crystal structure. Simultaneous recombination of the defects may occur, but a substantial number of point defects remains.<sup>14</sup> These radiation-induced defects drive microstructure evolution in nuclear fuel, both in and out of the reactor, which ultimately leads to degradation of thermal and mechanical properties.<sup>12</sup> Elucidation of the underlying mechanism for defect formation is of significant importance for understanding and predicting microstructure evolution under irradiation. One of the critical physical parameters for describing radiation damage in materials is the threshold displacement energy<sup>15</sup>  $E_d$ , which is the minimum amount of transferred kinetic energy necessary to permanently displace an atom from its original lattice site, thus, forming a stable defect, such as a Frenkel pair.

Experimentally, electron irradiation is utilized to produce point defects, and  $E_d$  is deduced from the threshold electron energy to produce a measurable response.<sup>16</sup> However, due to the short time and small length scales of the radiation events, a fundamental understanding of defect production at the atomic level is difficult to achieve. Theoretically, the threshold displacement energies can be calculated by applying the sudden approximation (SA) method<sup>17</sup> within the

classical Mott-Littleton approximation<sup>18</sup> or by the molecular dynamics (MD) method.<sup>13</sup> In the SA method, only static energy calculations are performed, and the dynamic effect of the primary knock-on atom (PKA) is not considered. The MD method is a good tool for understanding the atomic-level defect production mechanisms on picosecond time scales; however, the simulation results are strongly dependent on the quality of the interatomic potential employed and do not account for charge-transfer processes. In recent years, *ab initio* molecular dynamics methods in which the forces acting on the nuclei are calculated by electronic structure calculations rather than empirical fitting have proved to be a valuable tool for gaining insight on defect configurations produced by low-energy recoil events with *ab initio* accuracy.<sup>19–22</sup> In particular, the role of charge transfer during the dynamic process can be elucidated with this method.<sup>22</sup>

In ceramics, the crystal structures generally consist of multiple sublattices. Because the  $E_d$  strongly depends on orientation, the threshold displacement energy must be measured or determined computationally for each sublattice and for different crystallographic directions along which atoms are displaced. Consequently, the experimental measurement of this parameter in ceramics is relatively more difficult than in metals.<sup>16</sup> For pure cubic fluorite oxides, only the threshold displacement energies for UO<sub>2</sub> and CeO<sub>2</sub> are available in the literature. As listed in Table I, the mean-threshold displacement energies for UO<sub>2</sub> obtained by Meis and Chartier<sup>23</sup> using classical MD simulations are in reasonable agreement with the experimental values reported by Soullard and Alamo<sup>24</sup> and Soullard.<sup>25</sup> For CeO<sub>2</sub>, the classical MD simulation results reported by Guglielmetti *et al.*<sup>13</sup> also compare well with the electron irradiation experiments performed by Yasunaga *et al.*<sup>4</sup> Notwithstanding these studies, there are very limited data on the  $E_d$  values for the different sublattices in ThO<sub>2</sub> and ZrO<sub>2</sub>. The threshold displacement energies for yttria-stabilized zirconia (YSZ) have been investigated by Costantini and Beunee<sup>7</sup> and Costantini *et al.*<sup>26</sup> experimentally; however, the introduction of oxygen vacancies by Y doping causes different threshold irradiation responses in YSZ compared to pure zirconia, which is investigated here. At present, the radiation

TABLE I. Available experimental and theoretical threshold displacement energies (eV) for  $\text{UO}_2$ ,  $\text{CeO}_2$ , and YSZ in the literature.

	$\text{UO}_2$		$\text{CeO}_2$		YSZ	
	U	O	Ce	O	Zr	O
Exp.	$\sim 40$ (Soullard <sup>25</sup> )	$\sim 20$ (Soullard and Alamo <sup>24</sup> )	$44 \ll 58$ (Yasunaga <i>et al.</i> <sup>4</sup> )	$< 33$ (Yasunaga <i>et al.</i> <sup>4</sup> )	80 (Costantini and Beuneu <sup>7</sup> )	120 (Costantini and Beuneu <sup>7</sup> )
Calc.	$\sim 50$ (Meis and Chartier <sup>23</sup> )	$\sim 20$ (Meis and Chartier <sup>23</sup> )	56 (Guglielmetti <i>et al.</i> <sup>13</sup> )	27 (Guglielmetti <i>et al.</i> <sup>13</sup> )	80 (Costantini <i>et al.</i> <sup>26</sup> )	$> 200$ (Costantini <i>et al.</i> <sup>26</sup> )

damage processes in most ceramic oxides are not yet well understood, including the defect production mechanisms in cubic fluorite oxides.

In the present paper, an *ab initio* MD method is employed to study low-energy recoil events in  $\text{ThO}_2$ ,  $\text{CeO}_2$ , and  $\text{ZrO}_2$ . Because nanocrystalline  $\text{ZrO}_2$  is stabilized in the cubic fluorite structure without dopants and has broad applications,<sup>8</sup> the present paper includes undoped cubic  $\text{ZrO}_2$  rather than YSZ. Our main goal is to: (a) determine the threshold displacement energies for each cation and anion along specific crystallographic directions; (b) gain a fundamental insight on defect production processes and interactions in cubic fluorite oxides; (c) explore the role of charge transfer during the recoil events; and (d) compare the response behavior of  $\text{ThO}_2$ ,  $\text{CeO}_2$ , and  $\text{ZrO}_2$  to low-energy irradiation. The threshold displacement energies obtained from this study will be useful for determining relative defect production profiles using Monte Carlo simulations, for estimating relative damage production rates under electron, neutron, or ion irradiation, and for providing a means to normalize doses from various irradiation sources.<sup>27</sup>

## II. COMPUTATIONAL DETAILS

The *ab initio* MD calculations were carried out using the Spanish initiative for electronic simulations with thousands of atoms (SIESTA) code.<sup>28</sup> Since most physical properties of solids are dependent on the valence electrons to a much greater extent than on the core electrons, the pseudopotential approximation<sup>29</sup> is often employed in which the core electrons are removed and the strong nuclear potential is replaced by a weaker pseudopotential that acts on a set of pseudowave functions rather than the true valence wave functions. In this study, norm-conserving Troullier-Martins pseudopotentials<sup>30</sup> factorized in the Kleinman-Bylander form<sup>31</sup> were employed to describe the interaction between ions and electrons, and the exchange-correlation functional was determined within the

TABLE II. The reference electronic configurations for the Th, Ce, Zr, and O pseudopotentials and the pseudopotential core radii (Bohr).

	Electronic configuration
Th	$7s^2 (3.95) 7p^0 (3.95) 6d^2 (3.95) 5f^0 (3.95)$
Ce	$6s^2 (4.20) 6p^0 (3.40) 5d^2 (3.20) 4f^0 (2.80)$
Zr	$5s^2 (3.04) 5p^0 (3.19) 4d^2 (2.68) 4f^0 (2.68)$
O	$2s^2 (1.43) 2p^4 (1.43) 3d^0 (1.43) 4f^0 (1.43)$

generalized gradient approximation parametrized by Perdew *et al.*<sup>32</sup> The reference electronic configurations employed for the Th, Ce, Zr, and O pseudopotentials and the pseudopotential core radii are provided in Table II. All the simulations were conducted with a cell containing 324 atoms at a constant particle number and volume with periodic boundary conditions imposed along three directions. A cutoff energy of 130 Ry for the basis set and a  $K$ -point sampling of  $1 \times 1 \times 1$  in the Brillouin zone were employed. The valence wave functions were expanded in a basis set of localized atomic orbitals, and double- $\zeta$  basis sets were used. A variable time-step scheme was employed to avoid the instability of the simulations. The crystal was first equilibrated for 1000 time steps ( $\sim 1$  ps) at 100 K. An atom was selected as the PKA, and it was given a kinetic energy to initiate a recoil event. The maximum duration of each run was 1 ps. If the PKA returned to its original position at the end of the recoil event, the simulation was restarted at a higher recoil energy with an energy increment of 5 eV. Once the PKA was permanently displaced from its lattice site, additional runs were performed to improve the precision to 0.5 eV. After the PKA is permanently displaced, the system is then completely relaxed. For each atom type, recoils along four main crystallographic directions ([100], [110], [111], and [112]) were investigated in the present study as shown in Fig. 1. A Nose-Hoover thermostat was used in our simulations. In order to compare the radiation response of all the oxides with minimal reasonable computation effort, the random number seed was fixed when generating the velocities for all atoms. Hence, there are no statistics for threshold displacement energies.

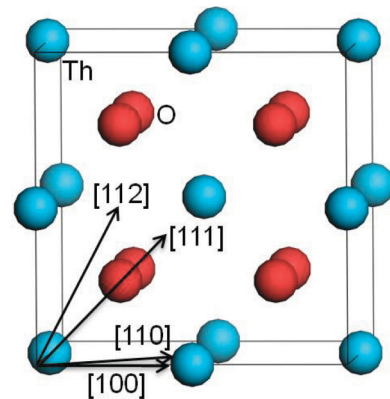
FIG. 1. (Color online) Schematic of the main crystallographic directions in fluorite  $\text{ThO}_2$ . Th and O atoms are indicated.

TABLE III. Comparison of ground-state properties for ThO<sub>2</sub>, CeO<sub>2</sub>, and ZrO<sub>2</sub> between our calculated values and experimental results from the literature.

	Lattice constant (Å)		Bulk modulus (GPa)		Cohesive energy (eV)		Band gap (eV)	
	Calc.	Exp.	Calc.	Exp.	Calc.	Exp.	Calc.	Exp.
ThO <sub>2</sub>	5.68	5.6 (Ref. 33)	258	278 (Ref. 33)	22.59	23.66 (Ref. 33)	4.05	5.75 (Ref. 50)
CeO <sub>2</sub>	5.45	5.41 (Ref. 34)	274	230 ± 10 (Ref. 34)	21.96	21.24 (Ref. 51)	2.98	3.0 (Ref. 52)
ZrO <sub>2</sub>	4.98	5.09 (Ref. 35)	225	194 (Ref. 37)	24.45	NA	3.56	6.1 (Ref. 53)

### III. RESULTS AND DISCUSSION

#### A. Ground-state properties for MO<sub>2</sub> (M = Th, Ce, and Zr)

In order to check the validity of the pseudopotentials employed in the present study, the lattice constants, bulk modulus, and cohesive energies for ThO<sub>2</sub>, CeO<sub>2</sub>, and ZrO<sub>2</sub> are calculated and are compared with available experiments. The results are summarized in Table III. It is shown that the calculated lattice constants for all the oxides agree well with experimental values.<sup>33–35</sup> The bulk modulus obtained by fitting the energy-volume curve for each oxide to the Murnaghan equation of state<sup>36</sup> are also in excellent agreement with experiments.<sup>33,34,37</sup> The cohesive energy for ZrO<sub>2</sub> is not available in the literature, and our result is purely predictive. It is noted that the cohesive energy for ZrO<sub>2</sub> is comparable to that for ThO<sub>2</sub> and CeO<sub>2</sub>. As for the band-gap values, our results are generally smaller than experimental values, except for CeO<sub>2</sub>, due to the well-known density functional theory underestimation.

#### B. Threshold displacement energies in MO<sub>2</sub> (M = Th, Ce, and Zr)

##### 1. Anisotropy of threshold displacement energies

The calculated  $E_d$  values for M and O PKAs along the main crystallographic directions in each oxide are summarized in Table IV and are compared in Fig. 2. The threshold displacement energies are found to be anisotropic for all recoil atoms. We find that, in each oxide, the minimum  $E_d$  values are along the ⟨110⟩ direction for M recoils and along the ⟨100⟩ direction for O recoils, and the highest values are along the ⟨111⟩ direction for both M and O recoils. These results are consistent with the linear atomic density trends of [110] > [100] > [111] for M and [100] > [110] > [111] for O.

In most cases, considerably higher energies are needed for displacing the M atoms than for displacing the O atoms. One exception is for the ⟨111⟩ direction, along which no defects are

generated for oxygen recoils even at energies of 100 eV. In this direction, the lattice atoms align in chains of Th<sub>1</sub>-O<sub>1</sub>-O<sub>2</sub>-Th<sub>2</sub> atoms, with a distance of 2.46 Å for ⟨Th-O⟩. Thus, for Th<sub>1</sub> and O<sub>2</sub> PKAs, their respective neighbors, i.e., O<sub>1</sub> and Th<sub>2</sub>, need to be displaced first in order to permanently form defects. For a recoil energy of 100 eV, the maximum transferred energy from Th to O (or from O to Th) is 24.1 eV, based on the conservation of momentum criteria. This transferred energy may displace an O from its lattice site by Th but is too small to displace a Th by O. Consequently, the threshold displacement energy for O along the ⟨111⟩ direction is much larger than that for Th. Because of the computational restrictions, further simulations of recoil events at energies exceeding 100 eV were not performed, and the exact threshold displacement energy values for O ions in the ⟨111⟩ direction are not yet determined.

##### 2. Comparison of calculated and experimental threshold displacement energies

Our prediction of  $E_d[111] > 100$  eV for O is supported by the classical MD simulations performed by Guglielmetti *et al.*,<sup>13</sup> who predicted a high  $E_d$  of 148 eV for O along the equivalent ⟨111̄⟩ direction. The threshold displacement energy of 56 eV for O along the ⟨100⟩ direction reported in their work<sup>13</sup> is also comparable to our result of 48.5 eV. In comparison with experiments, our minimum  $E_d$  of 46 eV for Ce along the ⟨110⟩ direction agrees well with the experimental values of 44–58 eV.<sup>4</sup> Moreover, the minimum  $E_d$  of 20 eV for O in CeO<sub>2</sub> along the ⟨100⟩ direction is within the reported experimental range of <33 eV.<sup>4</sup> To the best of our knowledge, no threshold displacement energies for pure zirconia have been reported in the literature. Experimental<sup>7</sup> and MD<sup>26</sup> studies reported  $E_d$  [001] values of 120 and >200 eV, respectively, for the O atoms and 80 eV for Zr atoms in YSZ, which are substantially higher than our results for pure ZrO<sub>2</sub>. This may arise from the direct role of the dopant in YSZ and the indirect role of the dopant-induced oxygen vacancies since 9.5 mol% Y<sub>2</sub>O<sub>3</sub> stabilized cubic ZrO<sub>2</sub> contains 4.75%

TABLE IV. Calculated threshold displacement energies (eV) along with available experimental data. YSZ: yttrium-stabilized zirconia.

	ThO <sub>2</sub>		CeO <sub>2</sub>		ZrO <sub>2</sub>	
	Th	O	Ce	O	Zr	O
[100]	53.5	17.5	48.5 [56 (Ref. 13)]	20.0	54.5	14.0
[110]	48.5	30.0	46.0	33.5	54.0	30.0
[111]	61.5	>100	63.0	>100 [148 (Ref. 13)]	68.5	>100
[112]	54.5	28.0	53.0	31.0	61.5	25.0
Exp.	NA	NA	44 ≪ 58 (Ref. 4)	<33 (Ref. 4)	80 (Ref. 7) (YSZ)	120 (Ref. 7) (YSZ)

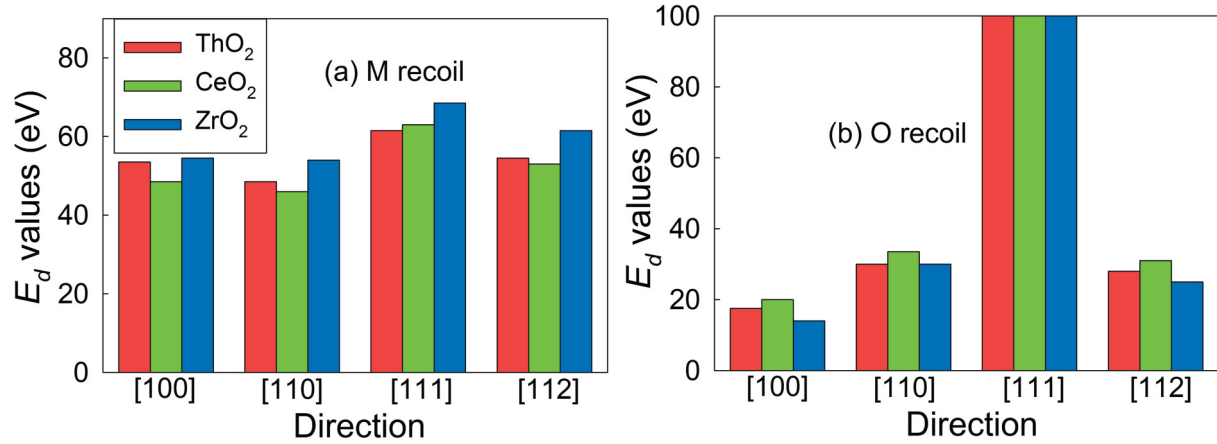


FIG. 2. (Color online) Threshold displacement energies ( $E_d$ ) for (a)  $M$  recoil and (b) O recoil in  $MO_2$  ( $M = \text{Th, Ce, or Zr}$ ).

oxygen vacancies. These vacancies, which situate adjacent to Zr atoms, reduce the symmetry and coordination of the Zr site<sup>38</sup> and affect the irradiation response of Zr. In the case of ThO<sub>2</sub>, no experimental or theoretical results are available for comparison. Comparing the results for ThO<sub>2</sub>, CeO<sub>2</sub>, and ZrO<sub>2</sub>, the threshold displacement energies for both  $M$  and O recoils in each oxide are generally comparable to each other. It is also noted that the experimental<sup>24,25</sup> and simulated<sup>23</sup> threshold displacement energies for UO<sub>2</sub>, as listed in Table I, compare well with our calculated results for ThO<sub>2</sub>, CeO<sub>2</sub>, and ZrO<sub>2</sub>.

### C. Defect generation for $M$ PKAs in $MO_2$ ( $M = \text{Th, Ce, and Zr}$ )

Table V summarizes the defects created after  $M$  recoil events in  $MO_2$  ( $M = \text{Th, Ce, and Zr}$ ) and the associated PKA displacement. It appears that, for a specific direction, the damage end states exhibit similar character to each other. In the case of  $M[100]$  and  $M[110]$ , the defects created are mainly  $M$  vacancies and  $M$  interstitials, whereas for  $M[111]$  and  $M[112]$  the neighboring oxygen atoms are also involved in the recoil events, resulting in the additional formation of oxygen vacancies and interstitials. The schematic of defect configurations for Th[100], Th[110], and Th[111] is illustrated in Fig. 3 and for  $M[112]$  is illustrated in Fig. 4.

When a kinetic energy of 53.5 eV is transferred to a Th atom along the  $\langle 100 \rangle$  direction, the Th PKA leaves its equilibrium site and collides with its first-neighbor Th atom [denoted as a secondary recoil atom (SRA)] along this direction. This process transfers sufficient energy to the SRA such that it is replaced by the PKA. The SRA moves further along the

same direction to form a stable octahedral interstitial in the center of the oxygen cube, as shown in Fig. 3(a), where it is coordinated to eight oxygens with a bond length of 2.39 Å. The Ce[100] and Zr[100] recoils also lead to a  $M$  vacancy and a  $M$  interstitial via the same pathway.

For the Th[110] with an energy of 48.5 eV, the PKA replaces its first-neighbor Th atom, which is subsequently displaced to an interstitial site, resulting in the formation of a Th vacancy and a Th interstitial. The Th interstitial is located at the bridge of two neighboring Th atoms in the  $\langle 110 \rangle$  direction and the bridge of two neighboring O atoms in the  $\langle 001 \rangle$  direction, pushing these atoms 0.61–0.98 Å away from their original sites. In the cases of Ce[110] and Zr[110], the mechanisms of defect generation show similar features to Th[110].

The low-energy recoil events along the  $\langle 111 \rangle$  direction are shown to be more complex than those along the  $\langle 100 \rangle$  and  $\langle 110 \rangle$  directions. A Th PKA along the  $\langle 111 \rangle$  direction, with an  $E_d$  of 61.5 eV, collides directly with its nearest-neighbor oxygen atom. The PKA passes through the oxygen site and heads for an octahedral site, forming an interstitial of the same type as that created by the  $M[100]$  case. The struck oxygen atom initially moves along the  $\langle 111 \rangle$  direction, while its trajectory is subsequently changed by the strong repulsive interaction between it and its neighboring atoms. This causes the oxygen atom to move along the  $\langle 112 \rangle$  direction and to occupy an octahedral interstitial site, where it is surrounded by six Th atoms with a distance of 2.69 Å and interacts with eight oxygen atoms at a distance of 2.64 Å. This results in final defect structures consisting of both Th and O vacancies and interstitials. Ce[111] exhibits nearly the same response to

TABLE V. The defects created after  $M$  recoil events in  $MO_2$  ( $M = \text{Th, Ce, and Zr}$ ) and the associated PKA displacement distance ( $d_{\text{PKA}}$ ).  $V_{\text{ion}}$ : ion vacancy;  $\text{ion}_{\text{int}}$ : ion interstitial.

$M$ direction	Th		Ce		Zr	
	Defect type	$d_{\text{PKA}}$ (Å)	Defect type	$d_{\text{PKA}}$ (Å)	Defect type	$d_{\text{PKA}}$ (Å)
[100]	$V_{\text{Th}} + \text{Th}_{\text{int}}$	5.22	$V_{\text{Ce}} + \text{Ce}_{\text{int}}$	5.01	$V_{\text{Zr}} + \text{Zr}_{\text{int}}$	4.80
[110]	$V_{\text{Th}} + \text{Th}_{\text{int}}$	3.09	$V_{\text{Ce}} + \text{Ce}_{\text{int}}$	2.88	$V_{\text{Zr}} + \text{Zr}_{\text{int}}$	2.66
[111]	$V_{\text{Th}} + \text{Th}_{\text{int}} + V_{\text{O}} + \text{O}_{\text{int}}$	4.76	$V_{\text{Ce}} + \text{Ce}_{\text{int}} + V_{\text{O}} + \text{O}_{\text{int}}$	4.42	$V_{\text{Zr}} + \text{Zr}_{\text{int}} + V_{\text{O}} + \text{O}_{\text{int}}$	3.99
[112]	$V_{\text{Th}} + \text{Th}_{\text{O}} + \text{O}_{\text{int}} + V_{\text{O}} + \text{O}_{\text{int}}$	4.58	$V_{\text{Ce}} + \text{Ce}_{\text{O}} + \text{O}_{\text{int}}$	4.46	$V_{\text{Zr}} + \text{Zr}_{\text{O}} + \text{O}_{\text{int}}$	3.93

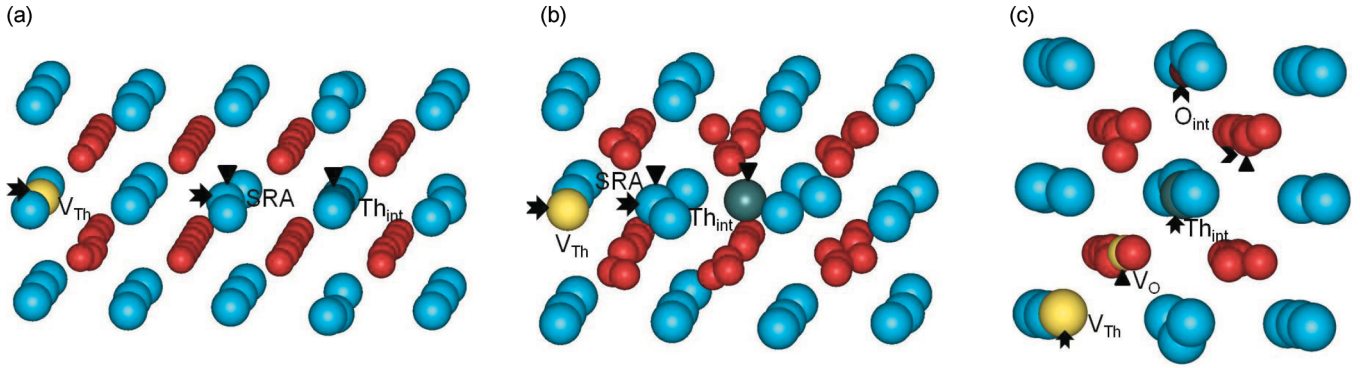


FIG. 3. (Color online) Schematics of the defect configuration on the Th sublattice for PKAs along the (a)  $\langle 100 \rangle$ , (b)  $\langle 110 \rangle$ , and (c)  $\langle 111 \rangle$  directions. The atom types are the same as those in Fig. 1. Yellow spheres represent vacancies, and dark blue or red spheres represent interstitials. The same types of arrows show the position of the corresponding atoms before and after the threshold event. SRA: secondary recoil atom.

low-energy irradiation as Th[111], whereas a slight difference is found for Zr[111] in which the struck oxygen keeps moving along the  $\langle 111 \rangle$  direction until it occupies an octahedral site. It is important to note that, whereas direct displacement of O atoms along  $[111]$  requires energies in excess of 100 eV,  $M$  recoils with energies less than 70 eV produce both  $M$  and O displacements.

Considering now the Th[112] direction, above 54.5 eV, the PKA collides with its first-neighboring oxygen with enough energy and replaces it to form an antisite,  $\text{Th}_\text{O}$ , defect. The replaced oxygen atom moves along the  $\langle 001 \rangle$  direction rather than the  $\langle 112 \rangle$  direction and substitutes for another oxygen atom, which moves toward an octahedral site to form a stable interstitial. This oxygen interstitial is of the same configuration as that generated by Th[111]. Furthermore, the oxygen atoms that are the first neighbors of the Th PKA also participate in the recoil events, as indicated by the elliptical line in Fig. 4(a), which leads to the creation of more oxygen vacancies and interstitials. Contrary to the case of Th[112], these first-neighbor oxygen atoms are not involved in the Ce[112] and Zr[112] recoil events, and there are no displacements for them

[see Figs. 4(b) and 4(c)]. Similar to Th, both the Ce and Zr recoils along  $[112]$  occupy vacant oxygen sites.

**D. Defect generation for O PKAs in  $\text{MO}_2$  ( $M = \text{Th, Ce, and Zr}$ )**

The defects created after O recoil events in  $\text{MO}_2$  ( $M = \text{Th, Ce, and Zr}$ ) and the associated PKA displacement distance are summarized in Table VI. It is interesting to note that, in all cases, the damage end state consists of only an oxygen vacancy and interstitial pair. Detailed analysis of the recoil events shows that, for a specific direction, the variation in the  $M$  atom from Th to Zr nearly has no influence on the mechanisms of defect generation. The representative defect configurations created by O PKAs in  $\text{ThO}_2$  along the  $\langle 100 \rangle$ ,  $\langle 110 \rangle$ , and  $\langle 112 \rangle$  directions are illustrated in Figs. 5(a)–5(c).

*1. Low-energy recoil events along different directions*

For an O PKA along the  $\langle 100 \rangle$  direction, a displacement sequence along the same direction is observed initially, and the last replaced oxygen atom then moves along the

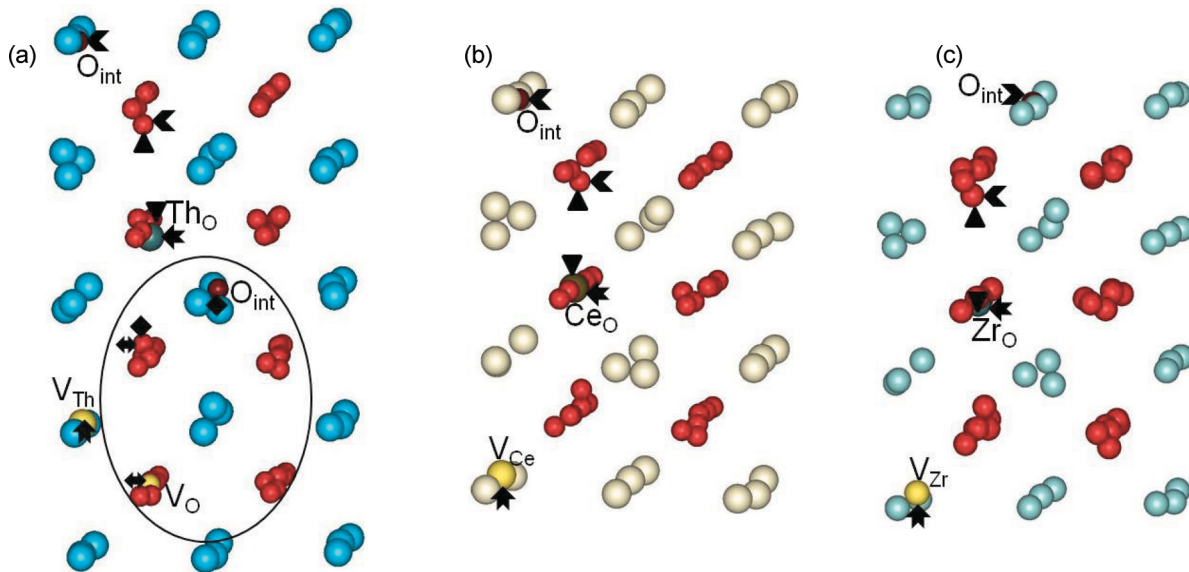


FIG. 4. (Color online) Schematics of the defect configuration on the (a) Th, (b) Ce, and (c) Zr sublattices for PKAs along the  $\langle 112 \rangle$  direction.

TABLE VI. The defects created after O recoil events in  $MO_2$  ( $M = \text{Th}, \text{Ce}, \text{and Zr}$ ) and the associated PKA displacement distance.  $V_O$ : oxygen vacancy;  $O_{\text{int}}$ : oxygen interstitial.

$M$ direction	Th		Ce		Zr	
	Defect type	$d_{\text{PKA}}$ (Å)	Defect type	$d_{\text{PKA}}$ (Å)	Defect type	$d_{\text{PKA}}$ (Å)
[100]	$V_O + O_{\text{int}}$	2.60	$V_O + O_{\text{int}}$	2.53	$V_O + O_{\text{int}}$	2.35
[110]	$V_O + O_{\text{int}}$	4.85	$V_O + O_{\text{int}}$	4.61	$V_O + O_{\text{int}}$	4.45
[112]	$V_O + O_{\text{int}}$	4.86	$V_O + O_{\text{int}}$	4.65	$V_O + O_{\text{int}}$	4.55

$\langle 1\bar{1}\bar{1} \rangle$  direction and eventually occupies an octahedral site, as illustrated in Fig. 5(a). In the case of the O[110] recoil, the energy barrier for defect formation along the  $\langle 110 \rangle$  direction is extremely high; consequently, the O PKA scatters toward the  $\langle 111 \rangle$  direction, along which the energy barrier is about 8.6 eV lower. This O PKA collides with one oxygen atom along the  $\langle 111 \rangle$  direction and replaces it, which moves along the  $\langle 001 \rangle$  direction and displaces another oxygen atom from its lattice site to occupy an octahedral interstitial site along the  $\langle \bar{1}\bar{1}\bar{1} \rangle$  direction. As for O[112], the PKA moves initially along the  $\langle 112 \rangle$  direction and then along the  $\langle 111 \rangle$  direction to replace one oxygen atom. The replaced oxygen atom moves along the  $\langle 1\bar{1}\bar{1} \rangle$  direction and, subsequently, occupies an octahedral interstitial site.

## 2. Interstitial site occupation for a recoil atom

In most studies on point defect properties in  $MO_2$  oxides, only the octahedral interstitials for  $M$  are taken into account.<sup>14,39,40</sup> Our *ab initio* MD simulations reveal that, besides the octahedral interstitial,  $M$  interstitials occupying the bridge site and vacant oxygen sites are also favorable, as shown in Figs. 3(b) and 4, respectively. As for the oxygen interstitial, it always occupies the octahedral site. Crocombette *et al.*<sup>40</sup> have investigated the stability of oxygen interstitials at: (1) an octahedral position in the center of the oxygen cube, (2) a position that is halfway from the octahedral site and from the line joining two adjacent oxygen atoms, and (3) a site that lies in the middle of the line joining the octahedral site and a summit of the oxygen cube. They found that the most stable oxygen interstitial position is the octahedral site, consistent with our results for  $\text{ThO}_2$ ,  $\text{CeO}_2$ , and  $\text{ZrO}_2$ . The oxygen interstitial near a sublattice oxygen atom, as suggested by the first-principles calculations of

Iwasawa *et al.* for  $\text{CeO}_2$ ,<sup>41</sup> is not observed in our simulations. Under irradiation, the formation of oxygen vacancies leads to  $\text{CeO}_2$  being partially reduced<sup>3,42</sup> from  $\text{Ce}^{4+}$  to  $\text{Ce}^{3+}$ . For  $\text{CeO}_2$  containing both  $\text{Ce}^{3+}$  and  $\text{Ce}^{4+}$ , the conventional density functional theory method describes its ground state incorrectly to be metallic, and the Hubbard- $U$  correction is necessary to localize the Ce  $4f$  electrons.<sup>3</sup> It should be pointed out that the Hubbard- $U$  correction for the on-site Coulomb interaction is not considered in the present study because such a correction is too computationally expensive to be taken into account, and the role of Ce  $4f$  electrons is neglected by assuming an electronic configuration of  $6s^2 6p^0 5d^2 4f^0$ . Such an assumption may affect the  $E_d$  values; however, as an initial step toward understanding the behavior of  $\text{CeO}_2$  under irradiation, our results provide useful information for related research and benchmarking MD results. For  $\text{ThO}_2$ , Th exhibits one oxidation state ( $\text{Th}^{4+}$ ) and contains no occupied  $5f$  states.<sup>43</sup> Similar electronic configurations have been employed for thorium ( $7s^2 7p^0 6d^2 5f^0$ ) and zirconium ( $5s^2 5p^0 4d^2 4f^0$ ) with ionic radii of 1.19 Å for  $\text{Th}^{4+}$  and 0.98 Å for  $\text{Zr}^{4+}$ . We find that, for both  $M$  and O PKAs,  $\text{ThO}_2$  and  $\text{ZrO}_2$  generally exhibit a similar low-energy irradiation response behavior, indicating that cation size plays a minor role in the behavior of fluorite oxides under irradiation.

## E. Charge transfer during the dynamic displacement process

One of the main advantages of the *ab initio* MD method is that it provides a fundamental insight into the role of charge transfer during the dynamic displacement process. The charge state of preexisting defects can be changed by simultaneous electronic and atomic collisions. Previous simulations of ion-solid interactions in SiC have revealed that significant charge transfer occurs during the dynamic process, and it

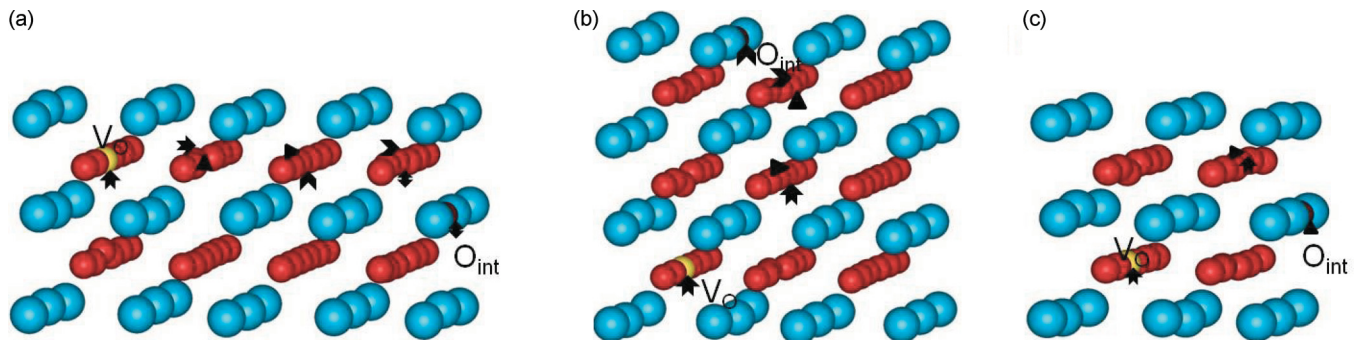


FIG. 5. (Color online) Schematics of the defect configuration on the O sublattice for PKAs along the (a)  $\langle 100 \rangle$ , (b)  $\langle 110 \rangle$ , and (c)  $\langle 112 \rangle$  directions.

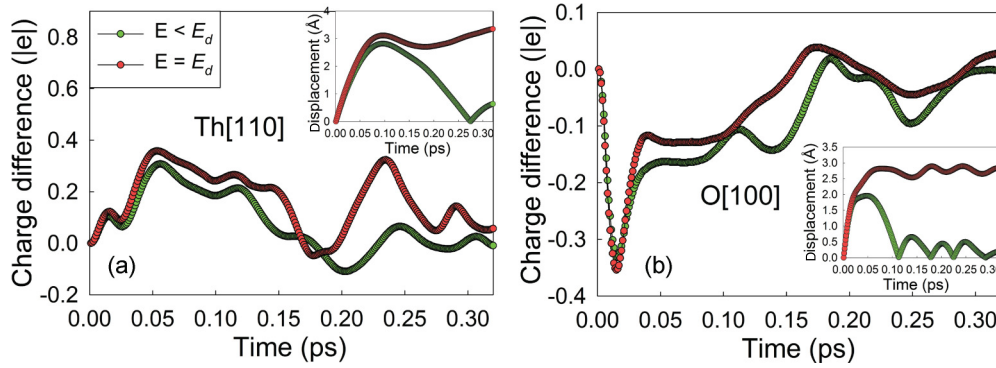


FIG. 6. (Color online) Variation in effective charge with time for (a) Th PKA along the  $\langle 110 \rangle$  direction and (b) O PKA along the  $\langle 100 \rangle$  direction at and below threshold displacement energies. The  $E_d$  values are 48.5 eV for Th[110] and 17.5 eV for O[100]. Insets show the PKA displacement distance as a function of simulation time.

can alter the energy barriers and dynamics for stable defect formation.<sup>22</sup> In the present paper, the role of charge transfer during the displacement process in ThO<sub>2</sub> is explored. Variation in effective charge differences for the Th PKA along the  $\langle 110 \rangle$  and O PKA along the  $\langle 100 \rangle$  direction as a function of time are illustrated in Figs. 6(a) and 6(b), respectively. The charges are relative to the effective charge of a Th or O atom in perfect ThO<sub>2</sub> and are obtained from Bader charge analysis. The calculated effective charge for Th and O in perfect ThO<sub>2</sub> are 2.68 and  $-1.34|e|$ , respectively. For both Th and O PKAs, the changes in effective charge at and below the threshold displacement energies are compared. It is found that charge gain and loss take place continuously during the whole dynamic process. At higher energies, more significant variation in the effective charge occurs to overcome the energy barrier for defect formation, suggesting that charge transfer plays an important role in determining the defect production process. This dynamic charge-transfer process may be responsible for the slightly lower values of  $E_d$  generally found by *ab initio* molecular dynamics compared to those determined by classical MD methods. The PKA displacement distance as a function of simulation time is shown in the Fig. 6

insets. The PKA returns to its original location at  $E < E_d$ , and a stable defect state is reached at  $E = E_d$ .

The charge-density difference  $\Delta\rho$  (i.e., the difference between a defective structure charge density and a superposition of atomic densities) in the plane that contains both the PKA and the vacancy is also determined. The  $\Delta\rho$  contours for defective structures created by Th[100] and O[112] recoil events are presented in Figs. 7(a) and 7(b), respectively. Taking the atomic charge density as a reference, it is clear that the Th vacancy and Th interstitial are negatively and positively charged, respectively. The Th interstitial interacts with neighboring oxygens and transfers electrons to them, causing them to be more negatively charged than other oxygen atoms. In contrast, there is a net decrease and increase in the electronic charge at the oxygen vacancy and interstitial sites, respectively, corresponding to positive and negative charge states. Upon oxygen vacancy formation, the charge of the host redistributes so as to screen the Coulomb potential due to the excess charge. It is found that the charge densities at both the Th and the O vacancy sites are more delocalized than those at the interstitial sites, indicating that the interactions between the vacancies and their neighbors are relatively stronger.

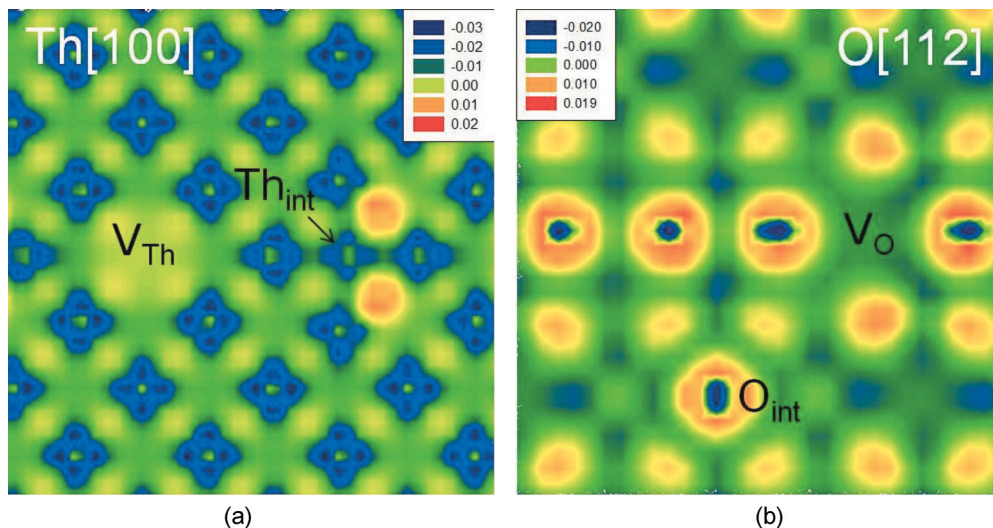


FIG. 7. (Color online) Charge-density differences for the defect states after (a) Th[100] recoil and (b) O[112] recoil.

It is well known that point defects in semiconductors or insulators may be charged rather than neutral. As a consequence, the charge states of point defects in metal oxides have been extensively studied.<sup>44–48</sup> Based on first-principles calculations, Crocombette *et al.*<sup>44</sup> suggested that the U vacancies in  $\text{UO}_2$  have the lowest formation energy for the  $-4$  charge state, and for O interstitials, the lowest formation energy corresponds to the  $-2$  charge state in most cases. The experimental studies performed by Garcia *et al.*<sup>49</sup> also showed that the O interstitials are doubly charged. As for the O vacancies, the preferred state depends on the position of the Fermi level. These results compare well with the theoretical studies of Nerikar *et al.*<sup>45</sup> Both theoretical calculations<sup>44,45</sup> considered not only isolated and noninteracting point defects as described above, but also point defect combinations, such as the Frenkel pair and Schottky defect. For oxygen Frenkel pairs, both studies show that the defects are made of double-positive vacancies and double-negative interstitials. In our calculations, the Bader charge for the Th and O interstitials are 2.3 and  $-1.23|e|$ , respectively, as compared with the charge of 2.68 $|e|$  for the Th and  $-1.34|e|$  for the O in perfect  $\text{ThO}_2$ . The differences in the charge for the oxygen interstitial between the present work and the calculations performed by Crocombette *et al.*<sup>44</sup> and Nerikar *et al.*<sup>45</sup> are due to the different methods employed. In their calculations of charged point defects, integral numbers of electrons are added or are removed from the system, resulting in a nominal charge of  $-2$  relative to the Bader charge for a stable O defect.

#### IV. CONCLUSION

Low-energy recoil events in  $\text{MO}_2$  ( $M = \text{Th}, \text{Ce}, \text{Zr}$ ) have been investigated by an *ab initio* MD method. The threshold displacement energies are found to be direction dependent. The minimum  $E_d$  values for Th, Ce, and Zr recoils are 48.5, 46, and 54 eV, respectively, which are all along the  $\langle 110 \rangle$

direction. For O recoils, the minimum  $E_d$  values are along the  $\langle 100 \rangle$  direction and vary from 14 to 20 eV. The highest values are all found to be along the  $\langle 111 \rangle$  direction for both  $M$  and O recoils. In most cases, considerably higher energies are needed for displacing the  $M$  atoms than for displacing the O atoms. One exception is for the  $\langle 111 \rangle$  direction, along which no defects are generated for oxygen recoils even at energies of 100 eV.  $\text{ThO}_2$ ,  $\text{CeO}_2$ , and  $\text{ZrO}_2$  generally exhibit similar low-energy irradiation response behavior, suggesting that the cation size has minor effects on the behavior of fluorite  $\text{MO}_2$  under irradiation.

The damage end states mainly consist of vacancies and interstitials. Of the interstitials, octahedral interstitials are found to be very stable, suggesting that they are main interstitial defects for  $\text{MO}_2$  under irradiation. Electronic structure analysis shows that charge transfer takes place during the whole dynamic process, and significant variation in the effective charge occurs to overcome the energy barrier for defect formation. This dynamic charge transfer may contribute to the slightly lower  $E_d$  values found by *ab initio* MD compared to MD methods. The charge redistribution leads to a negatively charged  $M$  vacancy. The created O vacancy is positively charged, which is caused by the delocalization of electrons on neighboring Th atoms. The  $M$  and O interstitials are found to be less positively and negatively charged, respectively, than the corresponding ions in perfect  $\text{MO}_2$ .

#### ACKNOWLEDGMENTS

This work was supported as part of the Materials Science of Actinides, an Energy Frontier Research Center funded by the US Department of Energy, Office of Science, Office of Basic Energy Sciences. The theoretical calculations were performed using the supercomputer resources at the Environmental Molecular Sciences Laboratory located at Pacific Northwest National Laboratory.

<sup>1</sup>A. Oaks, D. Yun, B. Ye, W. Y. Chen, and J. F. Stubbs, *J. Nucl. Mater.* **414**, 145 (2011).

<sup>2</sup>*Thorium Fuel Cycle-Potential Benefits and Challenges IAEA-TECDOC-1450* (International Atomic Energy Agency, Austria, 2005).

<sup>3</sup>H. Y. Xiao and W. J. Weber, *J. Phys. Chem. B* **115**, 6524 (2011).

<sup>4</sup>K. Yasunaga, K. Yasuda, S. Matsumura, and T. Sonoda, *Nucl. Instrum. Methods Phys. Res. B* **266**, 2877 (2008).

<sup>5</sup>W. J. Weber, *Radiat. Eff.* **83**, 145 (1984).

<sup>6</sup>Y. Zhang, P. D. Edmondson, T. Varga, S. Moll, F. Namavar, C. Lan, and W. J. Weber, *PhysChemChemPhys* **13**, 11946 (2011).

<sup>7</sup>J. M. Costantini and F. Beuneu, *Phys. Status Solidi C* **4**, 1258 (2007).

<sup>8</sup>Y. Zhang, W. Jiang, C. M. Wang, F. Namavar, P. D. Edmondson, Z. Zhu, F. Gao, J. Lian, and W. J. Weber, *Phys. Rev. B* **82**, 184105 (2010).

<sup>9</sup>T. Wiss, H. Matzke, C. Trautmann, M. Toulemonde, and S. Klumünzer, *Nucl. Instrum. Methods Phys. Res. B* **122**, 583 (1997).

<sup>10</sup>K. Hayash, H. Kikuchi, and K. Fukuda, *J. Nucl. Mater.* **248**, 191 (1997).

<sup>11</sup>K. E. Sickafus, H. Matzke, T. Hartmann, K. Yasuda, J. A. Valdez, P. Chodak III, M. Nastasi, and R. A. Verrall, *J. Nucl. Mater.* **274**, 66 (1999).

<sup>12</sup>D. S. Aidhy, D. Wolf, and A. El-Azab, *Scr. Mater.* **65**, 867 (2011).

<sup>13</sup>A. Guglielmetti, A. Chartier, L. v. Brutzel, J.-P. Crocombette, K. Yasuda, C. Meis, and S. Matsumura, *Nucl. Instrum. Methods Phys. Res. B* **266**, 5120 (2008).

<sup>14</sup>M. Freyss, T. Petit, and J.-P. Crocombette, *J. Nucl. Mater.* **347**, 44 (2005).

<sup>15</sup>H. Y. Xiao, F. Gao, and W. J. Weber, *J. Phys.: Condens. Matter* **22**, 415801 (2010).

<sup>16</sup>S. J. Zinkle and C. Kinoshita, *J. Nucl. Mater.* **251**, 200 (1997).

<sup>17</sup>R. D. Levine and R. B. Bernstein, *Molecular Reaction Dynamics* (Oxford University, New York, 1974).

<sup>18</sup>N. Mott and M. Littleton, *Trans. Faraday Soc.* **34**, 485 (1938).

<sup>19</sup>H. Y. Xiao, F. Gao, X. T. Zu, and W. J. Weber, *Phys. Rev. B* **80**, 212102 (2009).

<sup>20</sup>G. Lucas and L. Pizzagalli, *Phys. Rev. B* **78**, 045202 (2008).

<sup>21</sup>E. Holmström, A. Kuronen, and K. Nordlund, *Phys. Rev. B* **78**, 045202 (2008).

- <sup>22</sup>F. Gao, H. Y. Xiao, X. T. Zu, M. Posselt, and W. J. Weber, *Phys. Rev. Lett.* **103**, 027405 (2009).
- <sup>23</sup>C. Meis and A. Chartier, *J. Nucl. Mater.* **341**, 25 (2005).
- <sup>24</sup>J. Soullard and A. Alamo, *Radiat. Eff.* **38**, 133 (1978).
- <sup>25</sup>J. Soullard, *J. Nucl. Mater.* **135**, 190 (1985).
- <sup>26</sup>J. M. Costantini, F. Beuneu, S. Morrison-Smith, R. Devanathan, and W. J. Weber, *J. Appl. Phys.* **110**, 123506 (2011).
- <sup>27</sup>W. J. Weber *et al.*, *J. Mater. Res.* **13**, 1434 (1998).
- <sup>28</sup>J. M. Soler, E. Artacho, J. D. Gale, A. Garcia, J. Junquera, P. Ordejon, and D. S. Portal, *J. Phys.: Condens. Matter* **14**, 2745 (2002).
- <sup>29</sup>M. C. Payne, M. P. Teter, D. C. Allan, T. A. Arias, and J. D. Joannopoulos, *Rev. Mod. Phys.* **64**, 1045 (1992).
- <sup>30</sup>N. Troullier and J. L. Martins, *Phys. Rev. B* **43**, 1993 (1991).
- <sup>31</sup>L. Kleinman and D. M. Bylander, *Phys. Rev. B* **48**, 1425 (1982).
- <sup>32</sup>J. P. Perdew, K. Burke, and M. Ernzerhof, *Phys. Rev. Lett.* **77**, 3865 (1996).
- <sup>33</sup>P. J. Kelly and M. S. S. Brooks, *J. Chem. Soc., Faraday Trans.* **83**, 1189 (1987).
- <sup>34</sup>S. J. Duclos, Y. K. Vohra, A. L. Ruoff, A. Jayaraman, and G. P. Espinosa, *Phys. Rev. B* **38**, 7755 (1988).
- <sup>35</sup>C. J. Howard, R. J. Hill, and B. E. Reichert, *Acta Crystallogr., Sect. B: Struct. Sci.* **44**, 116 (1988).
- <sup>36</sup>F. D. Murnaghan, *Proc. Natl. Acad. Sci. USA* **30**, 244 (1944).
- <sup>37</sup>H. M. Kandil, J. D. Greiner, and J. F. Smith, *J. Am. Chem. Soc.* **67**, 341 (1982).
- <sup>38</sup>R. H. French, S. J. Glass, F. S. Ohuchi, Y.-N. Xu, and W. Y. Ching, *Phys. Rev. B* **49**, 5133 (1994).
- <sup>39</sup>M. Iwasawa, Y. Chen, Y. Kaneta, T. Ohnuma, H. Y. Geng, and M. Kinoshita, *Mater. Trans.* **47**, 2651 (2006).
- <sup>40</sup>J. P. Crocombette, F. Jollet, L. Thien Nga, and T. Petit, *Phys. Rev. B* **64**, 104107 (2001).
- <sup>41</sup>M. Iwasawa, T. Ohnuma, Y. Chen, Y. Kaneta, H.-Y. Geng, A. Iwase, and M. Kinoshita, *J. Nucl. Mater.* **393**, 321 (2009).
- <sup>42</sup>H. Ohno *et al.*, *Nucl. Instrum. Methods Phys. Res. B* **266**, 3013 (2008).
- <sup>43</sup>Y. Yun, P. M. Oppeneer, H. Kim, and K. Park, *Acta Mater.* **57**, 1655 (2009).
- <sup>44</sup>J.-P. Crocombette, D. Torumba, and A. Chartier, *Phys. Rev. B* **83**, 184107 (2011).
- <sup>45</sup>P. Nerikar, T. Watanabe, J. S. Tulenko, S. R. Phillpot, and S. B. Sinnott, *J. Nucl. Mater.* **384**, 61 (2009).
- <sup>46</sup>A. S. Foster, F. Lopez Gejo, A. L. Shluger, and R. M. Nieminen, *Phys. Rev. B* **65**, 174117 (2002).
- <sup>47</sup>I. D. Prodan, G. E. Scuseria, J. A. Sordo, K. N. Kudin, and R. L. Martin, *J. Chem. Phys.* **123**, 014703 (2005).
- <sup>48</sup>A. S. Foster, A. L. Shluger, and R. M. Nieminen, *Phys. Rev. Lett.* **89**, 225901 (2002).
- <sup>49</sup>P. Garcia, M. Fraczkiewicz, C. Davoisne, G. Carlot, B. Pasquet, G. Baldinozzi, D. Siméone, and C. Petot, *J. Nucl. Mater.* **400**, 112 (2010).
- <sup>50</sup>E. T. Rodine and P. L. Land, *Phys. Rev. B* **4**, 2701 (1971).
- <sup>51</sup>E. Voloshina and B. Paulus, *J. Chem. Phys.* **124**, 234711 (2006).
- <sup>52</sup>E. Wuilloud, B. Delley, W. D. Schneider, and Y. Baer, *Phys. Rev. Lett.* **53**, 202 (1984).
- <sup>53</sup>S. Kobayashi, A. Yamasaki, and T. Fujiwara, *Jpn. J. Appl. Phys.* **42**, 6946 (2003).